Modeling approaches in planetary seismology

Renee Weber, Martin Knapmeyer, Mark Panning, Nick Schmerr

Contents

List of illustrations *page* iv
List of tables v
List of contributors vi

1 Introduction 1

2 Site selection for future planetary seismology missions 2
2.1 The Moon 2
2.2 Mars 3

3 Sparse network or single-station seismology approaches 8
3.1 Event location by P-S differential time and back-azimuth 8
3.2 Event location via timing of surface wave orbits 9
3.3 Deep structure via normal mode analysis 10
3.4 Location capability for future lunar seismic networks 11

4 Exploring the relationship between lunar seismicity and tidal forcing 13

5 Seismic wavefield modeling 16
5.1 Normal mode seismology 16
5.2 Reflectivity and full wavefield methods 17

Illustrations

2.1	PKP ray fan and predicted amplitude.	4
3.1	Unique identification of deep moonquakes.	9
3.2	Location and origin time error histograms.	11
4.1	Normal tidal stress calculated at the A6 source location.	14
4.2	A1 grid search results.	14
5.1	Seismic structure of the lunar crust and megaregolith.	18
5.2	Seismic scattering in the lunar crust and megaregolith.	20

Tables

2.1 Marsquake recurrence times. 7

Contributors

1
Introduction

Of the many geophysical means that can be used to probe a planet's interior, seismology remains the most direct. Given that the seismic data gathered on the Moon over 40 years ago revolutionized our understanding of the Moon and are still being used today to produce new insight into the state of the lunar interior, it is no wonder that many future missions, both real and conceptual, plan to take seismometers to other planets.

To best facilitate the return of high-quality data from these instruments, as well as to further our understanding of the dynamic processes that modify a planet's interior, various modeling approaches are used to quantify parameters such as the amount and distribution of seismicity, tidal deformation, and seismic structure on and of the terrestrial planets. In addition, recent advances in wavefield modeling have permitted a renewed look at seismic energy transmission and the effects of attenuation and scattering, as well as the presence and effect of a core, on recorded seismograms. In this chapter, we will review these approaches.

2

Site selection for future planetary seismology missions

Typically, a minimum of three seismic stations is required for event location, and a fourth is required for depth determination. On Earth we take for granted that any given event will be relatively well-located, due to the comparative ease of installation of seismometers. For planetary applications, we cannot count on a large distribution of stations. Various factors including cost, difficulty of installation, instrumentation longevity, and data transmission severely limit the number of instruments that have been or will be deployed on other planetary bodies. In this section, we will review various methods that can be employed to help determine the best landing sites for future planetary seismology missions, in order to maximize their scientific return. We focus here on the Moon and Mars, although many of these methods are adaptable to other planetary bodies.

Key issues that feed into the site selection of future seismometer deployments include: 1) Theoretically establishing the seismicity and noise environment of a planetary body, including tectonic, volcanic, artificial, and natural impact sources; 2) Positioning of instruments relative to regions of expected seismic sources to maximize the detectability of important seismic waves that traverse the interior, including body, surface, and normal modes; and 3) Selection of landing sites and surface materials that maximize the longevity of a deployed instrument and minimize the seismic noise environment.

2.1 The Moon

The installation of seismometers on the Moon's surface during the Apollo era provided a wealth of information that transformed our understanding of lunar formation and evolution. Seismic events detected by the nearside network were used to constrain the structure of the Moon's crust and man-

tle down to a depth of about 1000 km. However, the lack of seismic ray paths penetrating the deepest Moon prohibited definitive identification of the Moon's core.

The presence of an attenuating region in the deepest interior, generally interpreted as a core, has been inferred from the paucity of farside events (Nakamura, 2005), as well as other indirect geophysical measurements (Wieczorek et al., 2006). In addition, more recent works have made progress in the recognition of core-reflected phases in the stacked Apollo data (Weber et al., 2011; Garcia et al., 2011). Such phases typically arrive in the coda of the main P and S arrivals, hampering their identification on individual seismograms.

Because the presence of a lunar core has important implications for the origin and evolution of the Moon, future missions should focus on refining our knowledge of the deepest interior. Weber et al. (2010) devised a technique to map ideal landing sites for the detection of core-interacting seismic phases from the known distribution of lunar seismic sources. The work focused on reflected (PcP, ScS) and converted (PKP) phases, but is easily adaptable to any seismic phase.

The method takes into account the predicted ray density and arrival amplitudes (Figure 2.1), as well as the level of seismicity from the known distribution of deep moonquakes. An example for the PKP arrival is illustrated in Plate 1A, using the velocity model of Nakamura (1983) modified to possess a core with radius 340 km and P-wave velocity of 5.0 km/s. At large epicentral distances, PKP is predicted as a first arrival, and hence should be easily identifiable on future seismograms.

2.2 Mars

The Viking landers of the late 1970's both carried a short-period three-component seismometer. On the Viking I lander, the un-caging mechanism failed to unlock the instrument. Viking II landed in Utopia Planitia and returned about 19 months of data (Lazarewicz et al., 1981); unfortunately because the seismometer was not coupled to the ground, it recorded only wind events (Anderson et al., 1977). Since Viking, several studies aimed to estimate the amount of seismicity that can be expected on Mars, in order to optimize future seismic experiments.

In general, three questions need to be answered to model a planets seismic activity:

1. How much deformation occurs in the lithosphere?

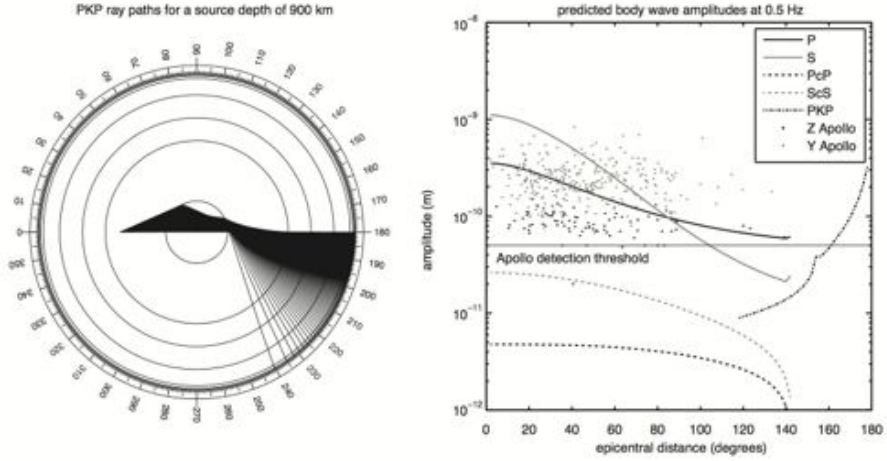

Figure 2.1 (left) Cross-section of the Moon showing the PKP ray fan for a source depth of 900 km. (right) Predicted arrival amplitudes for a number of seismic phases, including core-interacting phases. The dots show actual Apollo moonquake amplitudes. Note that core-reflected phases fall below the Apollo detection threshold. At large epicentral distances PKP is theoretically detectable by the Apollo seismometers, but such source-receiver geometries were lacking given the limited near-site extent of the array.

2. How does it translate into seismic events?
3. Where do these occur?

Philips (1991) analyzed several possible sources of deformation of the martian lithosphere. As no plate tectonics occur today on Mars, secular cooling of the planetary interior is the most important source of deformation, with an estimated annual seismic moment release of 4.8×10^{18}Nm, whereas tidal stresses can be neglected. Analyses of the accumulated slip visible on the martian surface today (Golombek et al., 1992; Golombek, 2002) yield moment release estimates of 10^{17}Nm and 10^{19} Nm per year.

Knapmeyer et al. (2006) investigated not only the total amount of moment release, but also its distribution among individual events and the distribution of these events over the planet. Their model is thus not only able to link the seismicity to geodynamic parameters but also able to produce synthetic event catalogs for the evaluation of seismic experiment concepts.

The model consists of three main parts. The annual moment release due to cooling of the lithosphere is first estimated. Then the moment-frequency relation (Gutenberg-Richter distribution) is modeled as a truncated pareto distribution, giving the number N of events that exceed a seismic moment

M_0. Finally, the seismic moment of an individual event is linked to the map length of the fault on which it occurred, by following the assumption that the stress drop is essentially constant for all quakes (e.g. Kanamori and Anderson, 1975). Knapmeyer et al. (2006) then mapped visible faults on the martian surface to distribute the individual event sizes according to the chosen distribution on faults that are long enough to produce them, i.e. small events may occur on almost any fault while large ones are restricted to the longest faults (Plate 1B).

Five scenarios were named to refer to the annual moment release (strong or weak) and the number of events (many or few) resulting from the Gutenberg-Richter distribution, with an average model that evenly distributed both factors. Translated into end-member magnitudes, the model suggests that the shortest fault ($L = 4$ km) can produce events with magnitudes up to $M_0 = 4.7$, while on the longest one ($L = 1445$ km), a $M_0 = 9.6$ event is possible. In other words, the whole annual budget of the weak/few scenario may be released in a single event on each of the mapped faults, while there is no severe restriction for the largest possible event from the size of tectonic features. The recurrence times for quakes of different size, according to the five model scenarios, are given in Table 2.1.

This seismicity model and the epicenter distributions derived from the mapped faults rely on a number of assumptions that may or may not be fulfilled. The amount of lithospheric contraction considered is based on a numerical simulation of the cooling of the lithosphere alone. Cooling of the entire mantle, the core, as well as a possible freezing of an inner core may modify the radius changes. The model for the distribution of events on the martian surface assumes that only the visible faults exist, and especially the possibility of deep sources is neglected. The latter is based on the assumption that deep quakes such as those that occur on subduction zones on Earth cannot occur in the absence of plate tectonics, and that the state of the martian mantle makes very deep sources similar to the lunar deep quakes impossible. The model by construction assumes that a strongest possible quake exists. The magnitude of this can of course be set to very high values. However, one must not confuse the annual seismic moment budget with the strongest possible event: the largest events observed on Earth release a seismic moment several times higher than the average annual release. Finally, the possibility of seismicity linked to volcanic activity is neglected: volcanism is a mechanism to cool the planetary interior, so active volcanism would change the cooling rates, and related events would occur near volcanic centers. These two effects were ignored because the current rate of martian volcanism ap-

pears to be too low to be of significance for a seismic experiment in the near future.

In addition to tectonic seismic events, impacts can also be used to study the interior of planets, and are expected to be relatively common on airless or thin atmospheric bodies throughout the Solar System. For the Moon, over 1700 impacts were recorded by the Apollo seismic array, translating to approximately one impact/day. Recent high resolution imaging of fresh craters on the surface estimates a similar cratering rate will be present on Mars (Daubar et al., 2013).

Table 2.1 *Recurrence times for marsquakes of different magnitudes, for five seismicity scenarios. The first row gives the annual seismic moment release. Moment magnitudes are limited by the assumption of a largest possible event. Units day (d) and year (a) refer to the respective durations on Earth.*

Mag. $M_w \geq$	Moment $M_0 \geq$	str./few	str./many	med.	weak/many	weak/few
	$M_{cum} =$	4.78×10^{18} Nm		5.99×10^{17} Nm	3.42×10^{16} Nm	
1	4×10^{10} Nm	38 min	72 s	48.5 min	2.5 h	3.9 d
2	1.3×10^{12} Nm	5.5 h	10.5 min	7 h	21.9 h	33.5 d
3	4×10^{13} Nm	1.9 d	1.5 h	2.5 d	7.9 d	290 d
4	1.3×10^{15} Nm	17.1 d	13.1 h	21.8 d	68.5 d	6.7 a
5	4×10^{16} Nm	148 d	-	189 d	-	50 a
6	1.3×10^{18} Nm	3.6 a	-	4.5 a	-	516 a
7	4×10^{19} Nm	30.3 a	-	-	-	$\sim$ 4500 a
7.6	3.2×10^{20} Nm	115 a	-	-	-	$\sim$ 17,000 a

3

Sparse network or single-station seismology approaches

Future planetary seismology missions are unlikely to have large numbers of instruments, as discussed previously. Therefore, many standard processing techniques used in terrestrial seismology will be ineffective for planetary applications. Specialized techniques are needed to analyze data from any future extraterrestrial seismic networks or single-station installations.

3.1 Event location by P-S differential time and back-azimuth

Future seismic missions to the Moon can take advantage of the known locations and depths of the deep moonquake clusters detected by Apollo, which are presumably still active today. Future instrumentation will record seismograms from these sources on N stations, and the P and S arrival times $t(P)$ and $t(S)$ from each station will result in $N \times 2$ unique observations. For a given event, we expect that with modern instrumentation we can measure $t(S) - t(P)$ with an accuracy of 5 seconds, back azimuth with an accuracy of 10 degrees, and the difference between the P arrivals at different stations with an accuracy of 1 second. With this information, we can map the clusters that can be uniquely identified using N desired landing sites. An example is shown in Figure 3.1 for $N = 2$.

Most of the clusters can be uniquely identified with the $S - P$ time difference and back azimuth. However, the remaining clusters can possibly be identified by including consideration of the temporal distribution of their occurrence times relative to the tidal cycle. All clusters could be identified uniquely with four or five stations in reasonable network geometry, simply by location. It is important to note that the number of unique identifications strongly depends on the positions of the stations relative to the clusters. Future landing sites should be chosen carefully to take advantage of established seismicity.

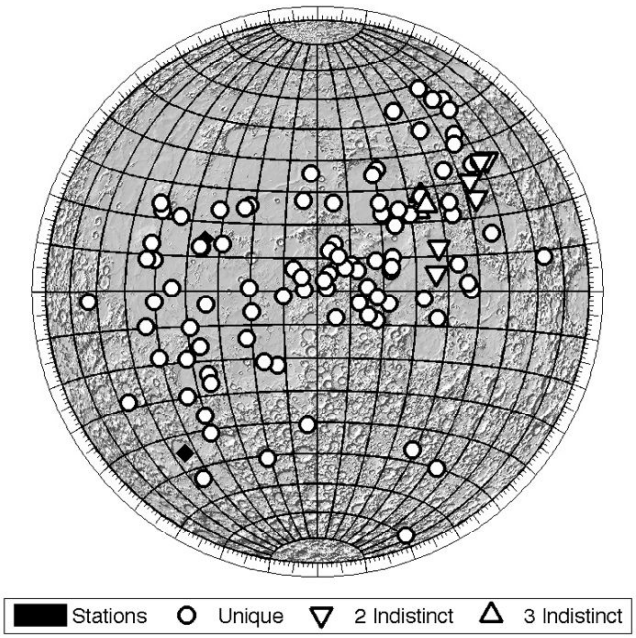

Figure 3.1 Number of neighbors with which a given deep moonquake cluster can potentially be confused. A large number of clusters can be uniquely identified using information from only two recording stations (diamonds). This number increases as the number of seismic stations increases.

3.2 Event location via timing of surface wave orbits

With a sufficiently large event where multiple orbit surface waves are recorded, epicentral distance and origin time can be determined at a single station without any requirement for an a priori velocity model. In the traditional surface wave numbering scheme, orbits are numbered such that the Rayleigh wave propagating along the minor arc is numbered $R1$, the wave propagating along the major arc is $R2$, and the wave that propagates along the minor arc with a complete great-circle orbit is numbered $R3$. If we filter data containing multiple orbit surface waves using a series of narrow band filters, and then measure the times of the $R1$, $R2$, and $R3$ peaks on the waveform envelopes, we can determine the great-circle averaged group velocity dispersion, epicentral distance, and event origin time using simple geometry.

For terrestrial data, we need events of approximately magnitude 6 in or-

der to reliably observe the weakest arrival, $R3$, but this approach can be extended to smaller events for smaller planetary bodies. Mars, for example, has a radius approximately half that of the Earth, and therefore $R3$ would be expected to be about an order of magnitude larger in amplitude simply due to geometric effects. A planet without an ocean would also likely have lower background seismic noise than the Earth (where the microseismic background noise is generated via ocean processes), and so multiple orbit surface waves will likely be measurable for magnitude 5 events on Mars with a high quality broadband seismometer, and possibly to lower magnitudes. This epicentral distance observation can be made independently in multiple frequency bands, which allows for some estimates of the error.

Provided the surface waves are adequately recorded on the horizontal components, we can also determine back azimuth using the elliptical particle motion of the Rayleigh wave by correlating rotated horizontal components with the Hilbert transform of the vertical component. Using such an approach with terrestrial data between magnitude 6 and 6.5, epicentral distance was constrained within a degree, and origin time within 30 seconds for most events, despite some biases due to un-modeled 3D structure (Figure 3.2). While such location errors would be large for the purposes of state-of-the art terrestrial seismology, initial tests show that they are adequate for performing velocity inversions using small numbers of P and S body wave picks, and resolve mantle velocity structure within 5%. Finally, the group velocity dispersion measurements included in this approach can then also be used to constrain shallow mantle structure using traditional surface wave dispersion modeling. This shallow structure then can allow better location of smaller events using S and P differential times as discussed previously.

3.3 Deep structure via normal mode analysis

For situations in which there is only a single deployed seismometer, another effective technique for studying deep structure is to use normal mode frequencies, which do not require knowledge of the source location. The periods of free oscillations of a planet are relevant to its structure. In particular the state of the core affects the fundamental modes of free oscillation, with the gravest spheroidal mode (${}_0S_2$) being the most sensitive.

Spectral peaks that are sensitive to mantle structure (520 mHz) can be detected at a noise threshold level of 10^{-9} $m/s^2/\mathrm{Hz}^{1/2}$, well within the capabilities of modern broadband seismometers being developed for planetary missions (Lognonne et al., 1996). A single large quake can excite a planet's normal modes, or multiple quakes with an equivalent cumulative seismic

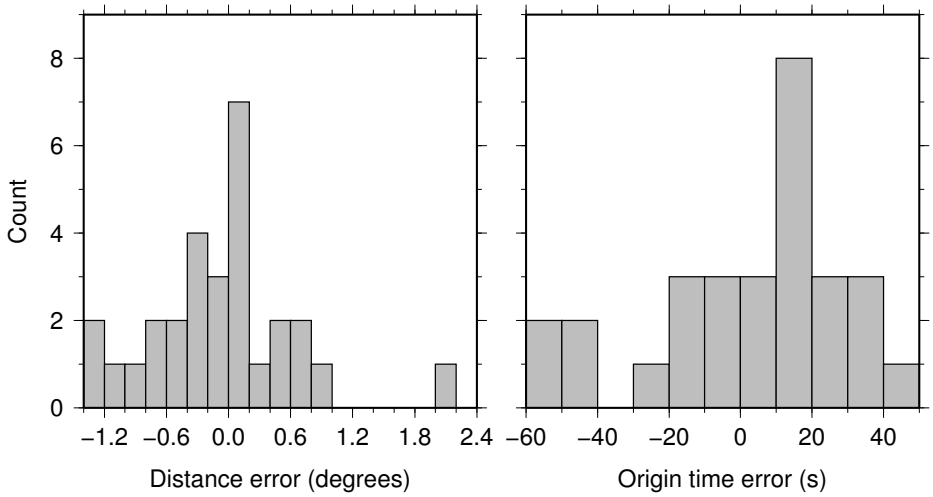

Figure 3.2 Histograms of epicentral distance errors (left) and origin time errors (right) for 29 events between magnitude 6.0 and 6.5 recorded at BFO in Germany, located by picking $R1 - R3$ arrival times. Positive errors represent distances that are too large, or origin times that are too late, respectively (Panning et al.; 2012).

moment can be stacked. Single-seismogram analysis requires a quake with seismic moment $\geq 10^{18}$ Nm, equivalent to a body wave magnitude mb ~ 6.

Khan and Mosegaard (2001) attempted to investigate lunar normal modes using Apollo seismic data recorded from large surface impacts, in order to constrain seismic velocities and densities in the deep lunar interior. Their observations were limited to the period during which the instruments were operated in "flat" mode, i.e. response extended to low frequencies; only five events during this time were large enough. Sufficiently large events on Mars are similarly predicted to be rare, with less than one event per year likely (Golombek et al., 1992; Knapmeyer et al., 2006); future seismic missions must rely on longevity to detect them.

3.4 Location capability for future lunar seismic networks

The traditional method for quake location converges towards the best-fit quake origin by minimizing the squared misfit between observed and theoretical travel times. This method assumes that arrival time readings are Gaussian-distributed. This assumption is problematic for data from sparse networks; a lack of redundancy means arrival time readings with large errors are more likely to be included in the solution.

The LOCSMITH event location scheme (Knapmeyer et al., 2008) was developed for sparse seismic networks on planets other than Earth. Rather than solving for a best-fit location, it divides the solution set into falsified and non-falsified candidate locations using an adaptive grid search, and accounts for arrival time uncertainty using windows around the true arrival time. The iterative algorithm starts with an icosahedral grid over all depths of the planet, refining the grid size on each iteration.

Hempel et al. (2012) applied the LOCSMITH algorithm to the Apollo seismic data. For a candidate set of grid points and detecting stations, theoretical travel times were calculated via ray-tracing using several different known lunar seismic velocity models. The travel times were then compared with observed arrival time windows for both compressional wave (P) and shear wave phases (S). The only assumption was that the chosen time window certainly contains the searched arrival, which is adequate for moonquakes given that the first arrivals are often emergent rather than impulsive.

If the gridded theoretical arrival times were found to lie within the arrival time windows for all stations and all phases, the grid point density around the corresponding grid point was refined for the next iteration. If not, the grid point was considered falsified. The solution sets of this algorithm are therefore clouds composed of all non-falsified grid points. The cloud size and shape depends on the number of observed arrivals. The best located clusters have ball-shaped clouds that are similar to traditional quake location error ellipses. Less well-located clusters have elongated clouds that resemble cones or bananas. The worst located clusters can only be constrained to disks that slice through the entire Moon.

This correlation between cloud shape and location uncertainty can be used to map the detection capability of future lunar seismic networks, assuming the known deep moonquake clusters are still active (and we have no reason not to expect them to be). Plates 1C and 1D shows the global location capability of an Apollo-like network, using a uniform distribution of 10,000 synthetic events. For a relatively small-aperture near side array consisting of Apollo-era instruments (Plate 1C), only events occurring in the vicinity of the network will be well-located (ball-shaped uncertainty clouds). For a globally-distributed network consisting of modern state-of-the-art instruments (10 times more sensitive than Apollo), there is a dramatic improvement in the location capability (Plate 1D).

4

Exploring the relationship between lunar seismicity and tidal forcing

As discussed in Chapter 4.5.1.5, deep moonquakes are known to occur periodically, with monthly (tidal) periodicity. To analyze the relationship between lunar seismicity and tidal forcing, several previous studies created models of the tidal stress field within the Moon. Solid-body tides are caused by the gravitational influence of the Earth, resulting in the deformation of the Moon such that moonquakes are caused or triggered in the deep interior.

In studies of tidal forcing, a key constraint is the focal mechanism: the fault parameters describing the type of failure moonquakes represent. Knowledge of the failure plane allows us to resolve the tidal stress into its shear and normal components and evaluate the state of stress at the observed moonquake occurrence times. The normal stress resolved onto an arbitrary fault plane calculated at the A6 deep moonquake source is shown in Figure 4.1. A6 moonquakes appear to occur at or near local minima in the normal stress, suggesting a relationship between moonquake occurrence and unloading on the fault.

In terrestrial seismology, the Coulomb stress criterion predicts failure when a linear combination of the shear and normal stress on a fault reaches some critical value. Weber et al. (2009) attempted to apply a similar criterion to deep moonquakes by searching for a fault orientation such that moonquakes occurred when a linear combination of shear and normal stress on that fault reached a constant threshold. The results of their attempt for the A1 source are shown in Figure 4.2. Fault orientations were searched in 10° increments of dip and strike. The linear combination C of normal and shear stress was computed on each fault plane such that the variance of the ratio between C computed at moonquake times and C computed on 1-day intervals was minimized. The absolute minimum of this variance ratio over all grid spaces was selected as the preferred fault plane.

This method worked better for some clusters than others, with a deep

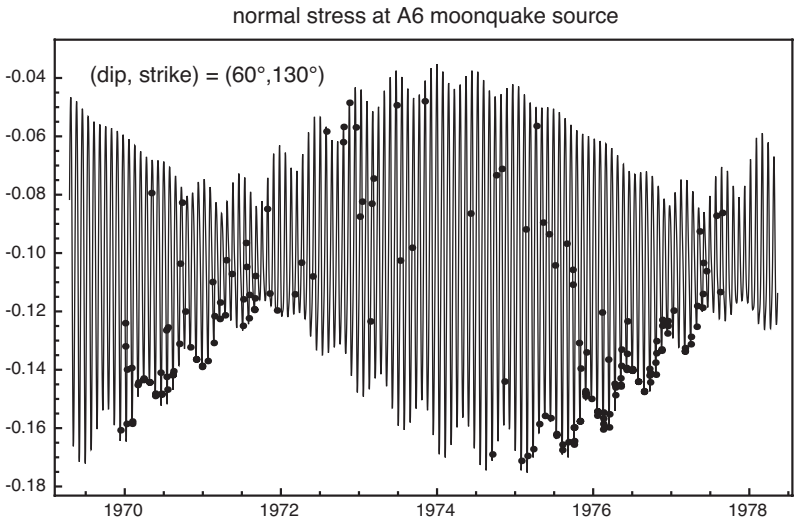

Figure 4.1 Normal tidal stress calculated at the A6 source location, on a fault with a dip of 60° and a strike of 130 deg, over the course of the Apollo experiment. Stress is calculated at one-day intervals (line) and at A6 moonquake times (dots). Vertical axis unit is bars.

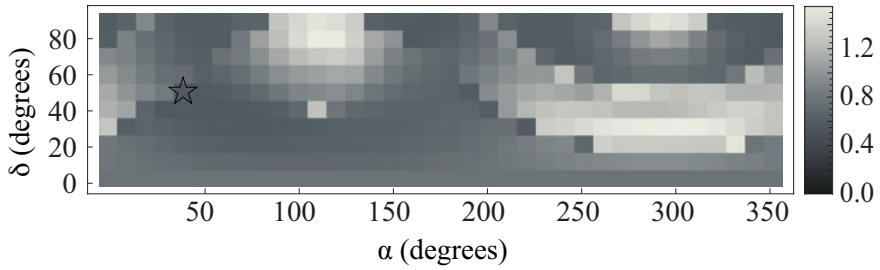

Figure 4.2 Variance ratio of the linear combination of shear and normal stress computed at A1 moonquake times to 1-day time steps, computed on a grid of all possible fault orientations. The best-fit fault plane occurs at the minimum variance ratio, and is indicated here with a star.

minimum around the best-fit solution. For others, the definition of the best-fit plane was more ambiguous, with a relatively shallow minimum, or several nearby minima in the strike-dip grid space. Since deep moonquake failure planes have no surface expression, there is no way to visually verify whether the best-fit plane is truly representative of the physical failure mechanism. In addition, the quality of the lunar seismic data combined with the limited source/receiver geometries of the Apollo network prohibit the determina-

tion of deep moonquake fault parameters using first-motion polarities, as is typically done in terrestrial seismology.

An alternative method for focal mechanism recovery examined the extent to which shear (S) and compression (P) wave amplitude ratios can constrain moonquake fault geometry by determining whether, for a given cluster, there exists a focal mechanism that can produce a radiation pattern consistent with the amplitudes measured by the Apollo instruments (Weber et al., 2012). Amplitudes were read in the ray coordinate frame, directly from seismograms for which the P and S arrivals were clearly identifiable on all long-period channels of the four Apollo stations. An empirical station correction accounted for site effects at the four Apollo stations, as well as the differences between P- and S-wave attenuation in the lunar interior.

Instead of focusing on the best fitting solution only (as in Weber et al., 2009), the inverse problem was formulated using a falsification criterion: all source orientations that do not reproduce the observed S/P amplitude ratios within an error margin derived from the uncertainty of the amplitude readings were rejected. All others were accepted as possible solutions. Similarly to the Weber et al. (2009) method, the inversion was carried out using a grid search with predefined step size, encompassing all possible combinations of fault strike and dip, but also included slip (the direction of fault motion between strike and dip).

Since the definition of a cluster implies that all events share the same source orientation, a combination of the inversion results of all events from one cluster reduces ambiguities in the inversion. Using only amplitude information, the fault plane parameter space for a given cluster was reduced on average by half (Plate 1E).

5

Seismic wavefield modeling

Lunar seismograms differ greatly from terrestrial seismograms. The low attenuation of seismic energy combined with the highly scattering environment in the shallow subsurface results in recordings that are emergent rather than impulsive, with long ringing coda that obscure all but the primary seismic phases. For this reason, it is useful to attempt to better understand the transmission of seismic energy within the Moon through wavefield modeling. In this section we will discuss different methods for synthetic seismogram generation, that are useful both for comparison with existing seismograms (the Moon) or for the prediction of seismic signals that might be recorded on other planets (Mars; Europa).

5.1 Normal mode seismology

Complete wavefields can be predicted efficiently using summation of normal modes calculated with *a priori* models of planetary structure. Such an approach is not well-suited for high frequency data, as the computations become more expensive and unstable for high frequencies and it is not trivial to include the effects of scattering and 3D structure, but they are extremely useful when predicting long period responses. Such calculations can be used in advance of particular planetary missions in order to explore likely candidate seismic signals for discriminating between models of planetary interiors.

For Europa, a moon of Jupiter, Cammarano et al. (2006) produced a range of possible thermodynamically consistent interior models by varying assumptions of initial chemistry, importance of tidal heating, and thickness of the ice shell overlying the likely global liquid water ocean (e.g. Kivelson et al., 2000). Panning et al. (2006) used these to create normal mode catalogs complete up to periods of 10 seconds. By analyzing synthetic seismograms from mode summation, it was determined that long period signals

from internal events analogous to deep lunar events would be unlikely to be recorded at the surface, but fracturing events in the ice shell would likely produce very strong signals with characteristics strongly dependent on the thickness of the ice shell. In the frequency band between 1 and 100 mHz, the fundamental mode Rayleigh wave undergoes a transition from a nearly non-dispersive wave at high frequencies, to a strongly dispersed flexural wave at lower frequencies. This flexural wave, also observed in terrestrial sea ice at higher frequencies (Press and Ewing, 1951), has a characteristic dispersion with phase velocity proportional to the square root of frequency, and group velocity equal to double the phase velocity. The transition between the non-dispersive Rayleigh wave and the flexural mode leads to a distinctive peak in group velocity at a frequency which depends on the thickness of the ice shell. This peak means that identification of a surface wave-train, even in the absence of event location, should be able to determine ice shell thickness simply by determining the frequency of the first-arriving Rayleigh energy.

5.2 Reflectivity and full wavefield methods

Seismic energy transmission in the Moon is governed not only by the very low attenuation of waves in the surface zone, but also the intense scattering and reverberation of waves in the low-velocity lunar megaregolith and regolith. These lowered seismic velocities are similar to those observed near impact craters on Earth, and are related to a high amount of pore space and fracture density lowering the rigidity and compressibility of impact brecciated materials (Figure 5.1a). Here we discuss methods to reproduce the long duration and pronounced coda observed in lunar seismic signals, and implications for seismic structure of planets/objects with surface megaregolith layers.

High frequency (>1Hz) synthetic wave propagation techniques are essential for properly replicating long duration codas that relate to scattering and reverberation of seismic energy within the megaregolith, which normal mode methods don't capture. Reverberations and trapping of seismic energy in a low-velocity wave channel can be achieved with a variety of 1-D wave propagation codes, but scattering requires a much more computationally expensive 3-D wavefield simulation, which has only recently become available. Below are two examples of how high frequency wave propagation methods can be used to investigate the effects of low-velocity surface wave guides and scattering in planetary surface materials.

Propagation of waves within the low-velocity surface materials can be approximated using a variety of 1-D seismic wave propagation codes. Typically these models allow specification of a layer-cake planet and are ef-

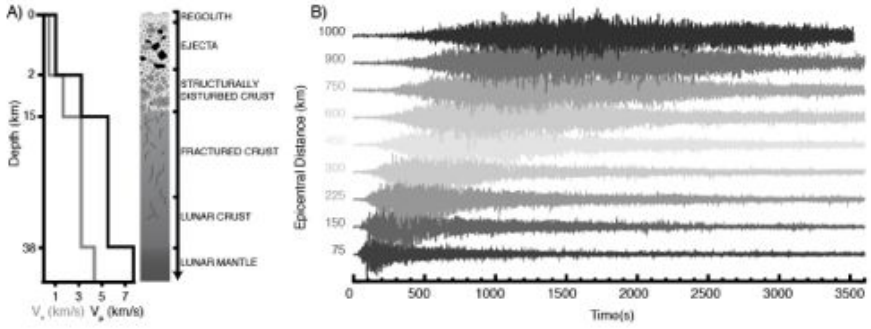

Figure 5.1 Seismic structure of the lunar crust and megaregolith. A) The crustal velocity model after Weber et al., (2011), showing the geology of the subsurface. The megaregolith extends from the surface to just above the structurally disturbed crust. B) 1-D wave propagation for a model with a 1 km thick layer of low-velocity megaregolith showing the development of surface waves and reverberations trapped in the layer.

ficiently run on modern CPUs at frequencies of ∼1 Hz. One example is GEMINI (Green's function of the Earth by MInor Integration), made available through the SPICE (Seismic wave Propagation and Imaging in Complex media: a European network) project. It solves the equations of motion for seismic source(s) and convolves the result with the Green's coefficients calculated for layered 1-D media. Source functions can be either empirically defined or from a standard set of basic source types. The code produces seismograms for anisotropic and anelastic media for any 1-D layer-cake model structure; responses are calculated for a user-defined set of stations at dominant frequencies up to 10 Hz. From 1-D simulations (Figure 5.1b) we can see that surface waves and multiple reverberations become trapped in the low velocities of the lunar megaregolith, serving as a waveguide for energy transmitted into this layer. This simulates the long duration of codas but does not fully replicate the scattering properties observed in the lunar megaregolith.

To properly address scattering, a high frequency, 3-D wave propagation code, such as WPP (Wave Propagation Program) is required (Petersson and Sjogreen, 2010). WPP solves the equation of motion on a 3-D finite difference, non-uniform Cartesian mesh, and is designed to run on parallel multi-CPU clusters. The user may specify elastic structures in 3D, including topography, layering, lateral heterogeneity, attenuation, and multiple sources with varying source time functions. The code is primarily used for regional simulations of wave propagation in complex media, the elastic response of

the medium is calculated for dominant frequencies up to 10 Hz or greater, though computational resources required grow for higher frequencies.

In Figure 5.2, we demonstrate the effect of scattering in the megaregolith using WPP to obtain lunar-like seismograms. By introducing a layer of scattering into the low-velocity megaregolith, several lunar-like wavefield features, including long duration codas, partitioning of energy on all three components of motion, and diffuse surface waves are reproduced. Additionally, body waves entering into the coda layer from below become scattered at the surface only. As computational resources grow, fully global simulations at high frequency are becoming available, allowing us to investigate the global effects of scattering at very long distances. Scattering effects will vary from world to world, with airless bodies with well-developed megaregoliths (Moon, Mercury, asteroids) having the highest proportion of scattering within their crusts relative to bodies with atmospheres and intragranular fluids and ices (Mars, Earth, Venus, the outer satellites). WPP is appropriate for any planetary object with a solid surface and can be used to approximate the scattering from rocky and icy worlds.

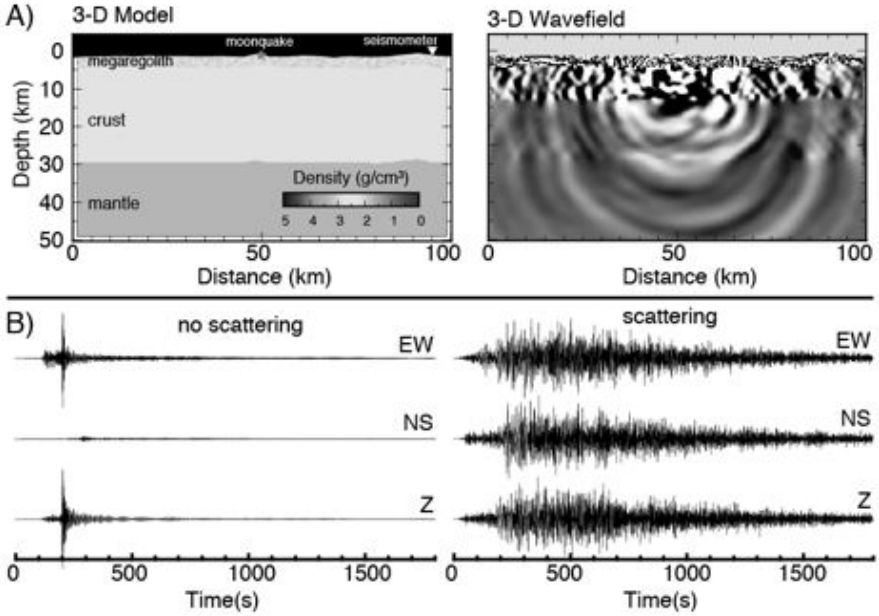

Figure 5.2 Seismic scattering in the lunar crust and megaregolith for an impact source. A) Cross section through a lunar model with 25%, 200 m scale-length, Von Karman random heterogeneity distribution (Frankel and Clayton, 1986) within a 3 km thick megaregolith and time snapshot of vertical displacement at 40 seconds into a WPP simulation. Positive amplitudes are black, negative white. B) Seismograms for a model with no scattering in the subsurface (left) and 25% heterogeneity (right) at 50 km from the source (location given in part A).

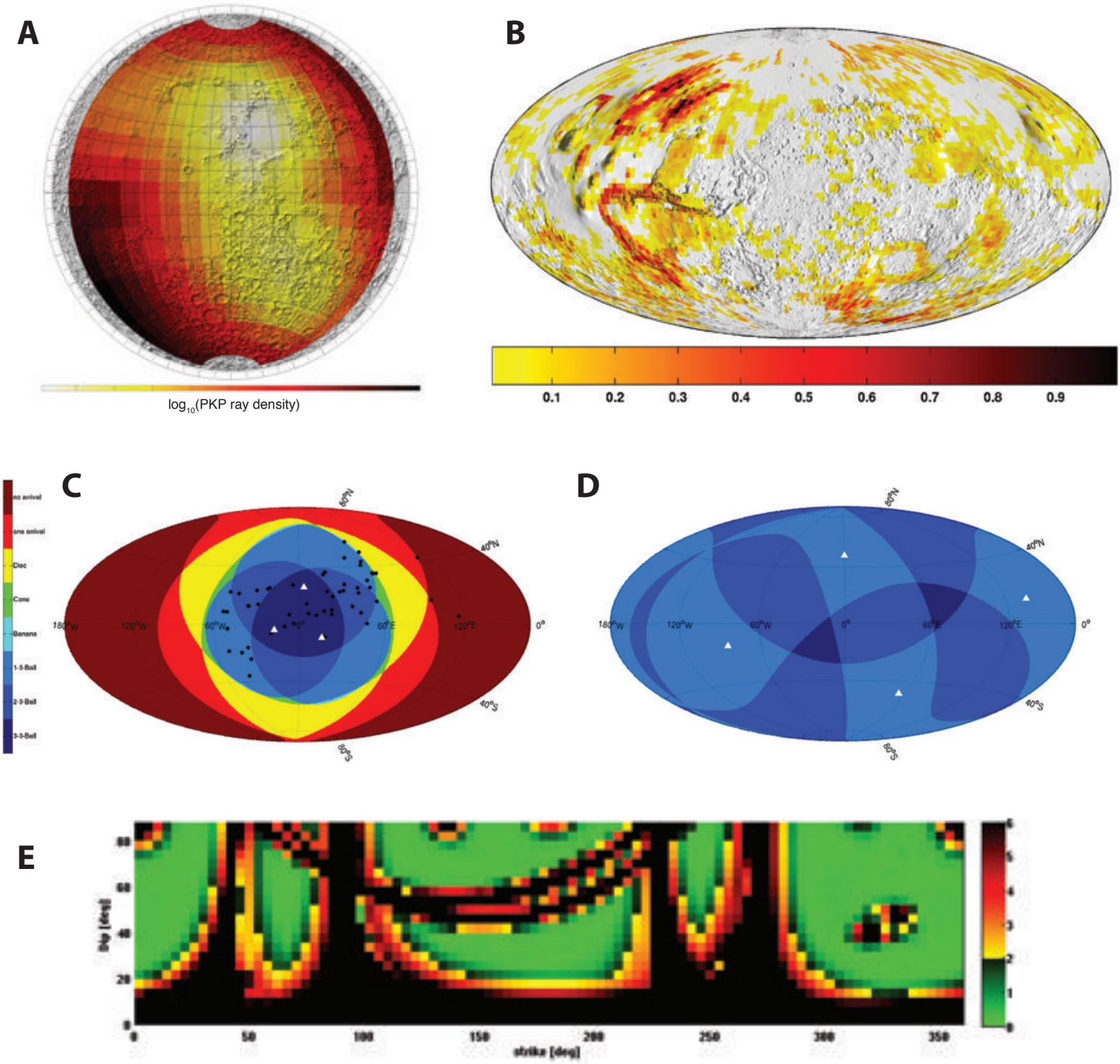

Plate 1. A) Nearside map of PKP ray density from the known distribution of deep moonquake clusters as a function of landing site coordinates, taking predicted cluster occurrence activity and arrival amplitudes into account, shown in logarithmic scale. For this particular phase, landing sites near the limb are favored, particularly in the southwestern quadrant of the Moon, where the likelihood of detecting PKP from the northeastern farside events is greatest. B) Map showing the probability that a $M_W \leq 4.8$ quake is assigned to 1 km^2 of surface, plotted on a 2.5º × 2.5º grid (Knapmeyer et al., 2006). C) Comparison between synthetically derived location clouds and the Apollo data, for an Apollo-like network. Dots represent ball-shaped located clusters of deep moonquakes. Triangles are station locations (Hempel et al., 2012). D) Location capability of a network with four equally distributed, state-of-the-art seismometers (Hempel et al., 2012). E) Least-squares misfit between observed and calculated amplitudes on a regular grid of fault orientations averaged over all useable events from the A6 source region. The accepted regions (green) are selected by highlighting fault orientations which predict amplitudes within two standard deviations of the measured values.

References

Anderson, D. L.; Miller, W. F.; Latham, G. V.; Nakamura, Y.; Toksöz, M. N.; Dainty, A. M.; Duennebier, F. K.; Lazarewicz, A. R.; Kovach, R. L.; Knight, T. C. D. (1977) *Seismology on Mars*. Journal of Geophysical Research 82, 4524 – 4546.

Cammarano, F.; Lekic, V.; Manga, M.; Panning, M. P.; Romanowicz, B. A. (2006) *Long-period seismology on Europa: 1. Physically consistent interior models*, Journal of Geophysical Res. 111, doi:10.1029/2006JE002710.

Daubar, I. J.; McEwen, A. S.; Byrne, S.; Kennedy, M. R.; Ivanov, B. (2013) The current Martian cratering rate. Icarus 225, 506 – 516.

Frankel, A., Clayton, R. W. (1986) *Finite difference simulations of seismic scattering: Implications for the propagation of short-period seismic waves in the crust and models of crustal heterogeneity*, Journal of Geophysical Research 91, 6465 – 6489.

Garcia, R.; Gagnepain-Beyneix, J.; Chevrot, S.; Lognonné, P. (2011) *Very preliminary reference Moon model*. Physics of the Earth and Planetary Interiors 188, 96 – 113.

Golombek, M. P.; Banerdt, W. B.; Tanaka, K. L.; Tralli, D. M. (1992) *A prediction of Mars seismicity from surface faulting*. Science 258, 979 – 981.

Golombek, M. P. (2002) *A revision of Mars seismicity from surface faulting*. Lunar and Planetary Science Conference XXXIII, Abstract #1244.

Hempel, S.; Knapmeyer, M.; Jonkers, A. R. T.; Oberst, J. (2012) *Uncertainty of Apollo deep moonquake locations and implications for future network designs*. Icarus 220, 971 – 980.

Kanamori, H.; Anderson, D. L. (1975), *Theoretical basis of some empirical relations in seismology*, Bulletin of the Seismological Society of America 65, 1073 – 1095.

Khan, A.; Mosegaard, K. (2001) *New information on the deep lunar interior from an inversion of lunar free oscillation periods.* Geophysical Research Letters 28, 1791 – 1794.

Kivelson, M. G.,; Khurana, K. K.; Russell, C. T.; Volwerk, M.; Walker, R. J.; Zimmer, C. (2000), *Galileo magnetometer measurements: A stronger case for a subsurface ocean at Europa*, Science 289, 1340 – 1343.

Knapmeyer, M.; Oberst, J.; Hauber, E.; Wahlisch, M.; Deuchler, C.; Wagner, R. (2006) *Working models for spatial distribution and level of Mars' seismicity*. Journal of Geophysical Research 111, doi:10.1029/2006JE002708.

Knapmeyer, M. (2008) *Location of seismic events using inaccurate data from very sparse networks*. Geophysics Journal International 175, 975 – 991.

Lazarewicz, A. R.; Anderson, D. L.; Anderson, K.; Dainty, A. M.; Duennebier, F. K.; Goins, N. R.; Knight, T. C. D.; Kovach, R. L.; Latham, G. V.; Miller, W. F.; Nakamura, Y.; Sutton, G. H.; Toksoz, M. N. (1981) *The Viking Seismometry Final Report*. NASA Contractor Report 3408, NASA Scientific and Technical Information Branch.

Lognonné, P.; Gagnepain-Beyneix, J.; Banerdt, W. B.; Cacho, S.; Karczewski, J. F.; Morand, M. (1996) *An Ultra-Broad Band Seismometer on InterMarsnet*. Planetary and Space Science 44, 1237 – 1249.

Lognonné, P.; Johnson, C. (2007) *Planetary Seismology*. Section 10.03 in *Treatises in Geophysics*, G. Shubert, ed., Elsevier.

Nakamura, Y. (1983) *Seismic velocity structure of the lunar mantle*. Journal of Geophysical Research 88, 677 – 686.

Nakamura, Y. (2005) *Farside deep moonquakes and deep interior of the Moon*, Journal of Geophysical Research 110, doi:10.1029/2004JE002332.

Panning, M. P.; Lekic, V.; Manga, M.; Cammarano, F.; Romanowicz, B. A. (2006) *Long-period seismology on Europa: 2. Predicted seismic response*, Journal of Geophysical Research 111, doi:10.1029/2006JE002712.

Petersson, N. A.; Sjogreen, B. (2010) *Reference guide to WPP version 2.0*. Lawrence Livermore National Laboratory Technical Report LLNL-TR-422928.

Phillips, R. J. (1991) *Expected rates of marsquakes*. Chapter in Scientific Rationale and Requirements for a Global Seismic Network on Mars, ed. Solomon, Lunar and Planetary Institute Technical Report #91-02.

Press, F.; Ewing, M. (1951) *Propagation of elastic waves in a floating ice sheet*, Eos Trans. AGU 32, 673 – 679.

Weber, R. C.; Bills, B. G.; Johnson, C. L. (2009) *Constraints on deep moonquake focal mechanisms through analyses of tidal stress*. Journal of Geophysical Research 114, doi:10.1029/2008JE003286.

Weber, R. C.; Garcia, R.; Johnson, C. L.; Knapmeyer, M.; Lognonne, P.; Nakamura, Y.; Schmerr. N. (2010) *The use of deep moonquakes for constraining the internal structure of the Moon*. Abstract U51B-0037 presented at 2010 Fall Meeting, AGU, San Francisco, California, 13-17 December.

Weber, R. C.; Lin, P.; Garnero, E. J.; Williams, Q.; Lognonne, P. (2011) *Seismic detection of the lunar core*. Science 331, 309 – 312.

Weber, R. C.; Knapmeyer, M. (2012) Deep moonquake focal mechanisms: recovery and implications. 43rd Lunar and Planetary Science Conference, Abstract #1466.

Wieczorek, M. A.; Jolliff, B. L.; Khan, A.; Pritchard, M. E.; Weiss, B. P.; Williams, J. G.; Hood, L. L.; Righter, K.; Neal, C. R.; Shearer, C. K.; McCallum, I. S.; Tompkins, S.; Hawke, B. R.; Peterson, C.; Gillis, J. J.; Bussey, B. (2006) *The Constitution and Structure of the Lunar Interior*. Reviews in Mineralogy and Geochemistry 60, 221 – 364.